

This is the accepted manuscript made available via CHORUS, the article has been published as:

Effect of Target Material on Fast-Electron Transport and Resistive Collimation

S. Chawla, M. S. Wei, R. Mishra, K. U Akli, C. D. Chen, H. S. McLean, A. Morace, P. K. Patel, H. Sawada, Y. Sentoku, R. B. Stephens, and F. N. Beg

Phys. Rev. Lett. **110**, 025001 — Published 7 January 2013

DOI: [10.1103/PhysRevLett.110.025001](https://doi.org/10.1103/PhysRevLett.110.025001)

Effect of target material on fast electron transport and resistive collimation

S. Chawla^{1,3}, M. S. Wei^{2,*}, R. Mishra¹, K.U Akli², C. D. Chen³, H. S. McLean³, A. Morace^{1,4},

P. K. Patel³, H. Sawada¹, Y. Sentoku⁵, R. B. Stephens², and F.N. Beg¹

¹ Center for Energy Research, University of California, San Diego, CA, USA

² General Atomics, San Diego, USA

³ Lawrence Livermore National Laboratory, Livermore, CA, USA

⁴ University of Milano Bicocca, Milan, Italy

⁵ University of Nevada, Reno, USA

The effect of target material on fast electron transport is investigated using a high intensity (0.7ps, 10^{20}W/cm^2) laser pulse irradiated on multi-layered solid Al targets with embedded transport (Au, Mo, Al) and tracer (Cu) layers, backed with mm-thick carbon foils to minimize refluxing. We consistently observed a more collimated electron beam (36% average reduction in fast electron induced Cu $K\alpha$ spot size) using a high- or mid- Z (Au or Mo) layer compared to Al. All targets showed a similar electron flux level in the central spot of the beam. Two-dimensional collisional particle-in-cell simulations showed formation of strong self-generated resistive magnetic fields in targets with a high-Z transport layer that suppressed the fast electron beam divergence; the consequent magnetic channels guided the fast electrons to a smaller spot, in good agreement with experiments. These findings indicate that fast electron transport can be controlled by self-generated resistive magnetic fields and may have important implications to fast ignition.

PACS: 52.38.Dx, 52.38.Hb, 52.50.Jm, 52.65.Rr

Cone guided fast ignition (FI) inertial confinement fusion requires efficient energy transport of high-intensity short-pulse-laser-produced relativistic (or "fast") electrons through a solid cone tip to a high density fuel core [1]. Specifically, successful ignition with a reasonably sized ignition laser requires high conversion efficiency to 1-3 MeV electrons that have a minimum divergence [2, 3]. Previous simulations show that fast electron beam propagation in solid density plasmas are affected by a variety of mechanisms: scattering, resistive collimation [2, 4], resistive filamentation [5], ohmic heating and electric field inhibition [6, 7]. Evaluating the cone tip material, therefore, requires an understanding of the evolution of self-generated resistive fields and their cumulative effect on electron transport over the duration of the laser pulse. Previous material dependent transport studies are limited; They have studied transport through only one material [8, 9], simultaneously varied materials and fast electron sources [10, 11], or used energies much lower than presented here [11, 12].

In this Letter, we report a systematic investigation of fast electron transport in different materials (from high-Z Au to low-Z Al) without changing the electron source. We have demonstrated that a fast electron beam can be collimated with a thin ($\sim 10\mu\text{m}$), high- or mid-Z transport layer buried a few μm beneath a low-Z Al layer without imposing a significant loss in forward-going electron energy flux, in contrast to previous 1D Fokker-Planck (FP) modeling predictions [13] that suggest high-Z Au material would increase divergence due to scattering and reduce the forward energy coupling, but consistent with the analytical model and 2D FP modeling showing stronger resistive collimation in high-Z plasmas by Bell and Kingham [4]. In addition, the collimation did not rely on complex structured targets [14] or a double laser pulse configuration [15], as shown in recent experimental work. $K\alpha$ fluorescence diagnostics, similar to those used in earlier work by Stephens et al. to measure fast electron beam divergence [16], directly characterized fast electron density distributions within the target. 2D collisional PIC simulation results are in excellent agreement with experiments and show the formation, in high-Z transport targets, of strong resistive magnetic channels enveloped by a global B-field that collimate initially divergent fast electrons. These magnetic channels extend into the subsequent lower resistance layers, maintaining the guidance of fast electrons.

The experiment used the Titan laser ($1\mu\text{m}$ wavelength, 150J in 0.7ps, 17mJ average prepulse energy in 2.3ns) at the Jupiter Laser Facility, Lawrence Livermore National Laboratory. An $f/3$ off-axis parabola

focused the beam to a $10\mu\text{m}$ (FWHM) spot with an incident angle of 17° onto the target front surface at $I_{\text{peak}} \sim 10^{20} \text{W/cm}^2$. Figure 1 shows a schematic of the multilayered solid target, laser beam and x-ray diagnostics. Targets had a common Al front layer ($3\mu\text{m}$ thick), a Z-transport layer {Au ($8\mu\text{m}$), Mo ($14\mu\text{m}$) or Al ($33\mu\text{m}$)}, and a Cu tracer layer ($22\mu\text{m}$) buried $110\mu\text{m}$ behind the Z-transport layer. The common front Al layer for all targets was to provide an identical fast electron source for the transport study. The Z transport layer thicknesses were chosen to have similar shock transit times; in cone-guided FI they would provide equivalent protection from implosion driven shocks. $K\alpha$ fluorescence from the Cu layer was used to characterize the fast electrons. The transverse dimensions of these layers were $1 \times 1 \text{mm}^2$. A conductive carbon layer (1mm thick, $5 \times 3 \text{mm}^2$ transversely) at the back of the target was used to minimize electron refluxing [17].

The cross-section for $K\alpha$ fluorescence is relatively constant for wide range of electron energies [18, 19] and therefore Cu K-shell emission intensity correlates well with fast electron flux [20]. This fluorescence was imaged with a narrow bandwidth (6eV centered on 8048eV) spherically bent quartz crystal [21] with a 50mm radius of curvature (Fig. 1). The image magnification was 6 and the spatial resolution was $20\mu\text{m}$ using Fuji image plates as detectors. An absolutely calibrated flat crystal spectrometer [22] using a highly ordered pyrolytic graphite (HOPG) diffraction crystal was also used to measure the spatially integrated total Cu $K\alpha$ yield.

The $K\alpha$ imager consistently recorded smaller Cu $K\alpha$ spots from targets containing either Au or Mo transport layers as compared to the Al targets. Figures 2(a) and 2(b) show typical images for the Z=Au and Z=Al transport targets while Fig. 2(c) shows the corresponding radial $K\alpha$ intensity profiles, averaged over 2 data points per material, for the same main laser pulse and prepulse conditions. Analysis of these profiles shows that the $K\alpha$ spot sizes (FWHM) in Au ($96 \pm 20 \mu\text{m}$) and Mo ($84 \pm 20 \mu\text{m}$) cases are, on average, 36% smaller than that of the Al ($140 \pm 20 \mu\text{m}$) targets and the $K\alpha$ signal reduction occurs mostly in the wing region. Integrating under different parts of these curves allows us to examine spatial variations in the electron flux. Within a $20\mu\text{m}$ radius we calculate a 20% reduction of electron flux in the Au transport targets as compared to the Al targets. The lower and upper bounds of this reduction were 1% and 33%, respectively, given the variation in the data as shown by the shaded area in Fig. 2(c). The same

calculation for a 170 μm radius gives a reduction of 56% with lower and upper bounds of 41% and 72%. The reduction in the integrated $K\alpha$ signal at large radii is consistent with the reduction in the total $K\alpha$ yield measured by the HOPG x-ray spectrometer as shown in Fig 2(d). The $K\alpha$ yield reduction by a factor of 2 cannot be explained simply by the increase of ionization energy in the high-Z material. Resistive stopping by strong resistive E-fields and B-field trapping seem to be the main cause of the electron flux reduction in the high-Z transport material, as discussed in more detail below. It should also be noted that signal variation (20% reduction) in the central 20 μm radius region is within our measurement error. It is reasonable to say, then, that although the total $K\alpha$ yield is reduced for the Au and Mo transport targets, $K\alpha$ signal (and therefore fast electron flux) in the central 20 μm radius spot remains the same for all targets.

To understand the underlying transport physics in this experiment, 2D collisional Particle in cell (PIC) simulations have been performed using the PICLS code [23], a fully relativistic kinetic code that self-consistently models laser-plasma interactions and subsequent energy transport. Simulations include dynamic impact ionization, radiative losses and a relativistic binary collision model that incorporates collisions between free-free and free-bound electrons (particularly necessary to accurately reproduce energy transport in a high Z partially ionized medium). A Gaussian laser pulse (1 μm , 726fs, 10 μm spot, $I_{\text{peak}} \sim 9 \times 10^{19} \text{W/cm}^2$) is normally incident on the target front surface. The solid density targets have a transverse dimension of 160 μm with layers of (I) Al+Z(Al)+Al, each with uniform density and thicknesses of 3+33+4 μm or (II) Al+Z(Au)+Al, also uniform, with thicknesses of 3+8+9 μm . The front target surface is preceded by a 10 μm long Al preplasma with a density varying from 2×10^{20} to $1.2 \times 10^{22} \text{cm}^{-3}$ with a 1/e scale-length of 2 μm . This preplasma profile is obtained from 2D radiation hydrodynamic modeling using the HYDRA code [24] with the experimentally measured laser prepulse conditions. The ion density for Al (Au) is set to $56n_c$ ($50n_c$) according to its mass density, 2.7g/cc (19.7g/cc), where n_c is the critical density for 1 μm wavelength light. The initial ionization charge state is set to +3 (+4) for Al (Au). Absorbing boundary conditions are applied for fields and particles (i.e., no fast electrons re-circulated back into the target).

We first examine the simulated electron energy density and electron flux profiles for comparison with the experimental $K\alpha$ data. Comparison of the contour plots of the electron energy density shows that fast electron beam transport in the Z=Au target (Fig. 3(b)) is clearly more collimated than in the Al target

(Fig. 3(a)), consistent with the experimental $K\alpha$ data. Note that the electron source produced from the laser interaction with the Al preplasma in both cases is identical and has a large source divergence ($\approx 50^\circ$ half angle) as a result of critical surface deformation by the intense laser pressure [25]. Fig 3(c) is the time integrated electron flux distribution, from which the calculated ratio of the FWHM of the fast electron spot from the Al target to that of Au is 1.47, in excellent agreement with the experimental $K\alpha$ spot size ratio of 1.55. It also confirms that the reduction of electron flux mainly occurs in the wing region (outside the central $20\mu\text{m}$ radius) while the flux in the center spot is maintained, exactly the same trend observed in the experiment. Electron angular spread denoted by the mean propagation angle (Fig. 3(d)) shows a significant reduction in electron beam divergence inside the Au transport target within the central region.

The observed difference in fast electron beam transport can be explained by the corresponding self-generated resistive magnetic fields as a result of different resistivity evolutions in these two types of targets. The growth of the self-induced magnetic field is determined by $\partial \vec{B} / \partial t = -\vec{\nabla} \times \vec{E} = -\vec{\nabla} \times (\eta \vec{J}_R)$, where J_R is the return current excited to neutralize the fast electron current (\vec{J}) and η is background plasma resistivity. In our simulation geometry, the dominant terms for azimuthal B-field generation are given by:

$$\partial \vec{B}_z / \partial t = \eta (\partial \vec{J}_x / \partial y) + (\partial \eta / \partial y) \vec{J}_x \quad (1)$$

Note that resistivity in the PICLS modeling results from binary collisions between different species and follows the Spitzer behavior ($\eta \propto Z / T^{3/2}$), except for the cold plasma ($< 10\text{eV}$) in degenerate regime where the collision frequency is kept constant [23]. Fig. 4 compares the quasi-static azimuthal B_z fields in Al and Au transport targets at both an early time (198fs) and later time (end of the laser pulse, 726fs). Note that a high-intensity-laser-produced fast electron beam ($> \text{Mega-Ampere}$ current) is subjected to the resistive filamentation instability when traveling through a charge and current neutralizing background [5]. This instability tends to destroy the local current neutralization causing the beam to breakup into multiple self-guided current channels. At an early time (198fs), similar diverging electron beam and filamented field structures (Fig. 4 (a) and (b)) are observed in both Al and Au transport targets. With the rapid ionization and heating of the Al target, the resistivity drops in the center region where current

density is high and thus the two terms on the RHS of Eq. 1 oppose each other and limit field growth. Relatively weak magnetic fields ($B_z \approx 5\text{MG}$) allow the fast electron beam to continue to propagate ballistically inside the Al target maintaining its source divergence over the laser duration, as shown in plots of B_z (Fig. 4(c)) and electron energy density (Fig. 3(a)). This is consistent with the fast electron mean propagation angle plot in Fig. 3(d) showing that the fast electron beam spreads out with propagation distance inside the Al transport target. In contrast, plasma resistivity and B-field dynamics are more complex in the Au transport target. Due to large heat capacity and high atomic number, Au plasma resistivity in the center of the high current remains high and the resistive field growth is dominated by the first term of the RHS of Eq. 1. Resistive magnetic fields as strong as 60MG are produced when the laser pulse is still at its rising stage near the peak intensity. In such intense fields the Larmor radius, $r_L (\mu\text{m}) \approx 30E_{\text{MeV}}/B_{\text{MG}}$, of $\approx 3\text{MeV}$ electrons is $\approx 1\mu\text{m}$. Thus, we expect significant guiding and collimation of fast electrons in the magnetic channels. This is indeed evident in Fig. 4(d) where we observe a few current channels of width $\approx 3\mu\text{m}$ in the Au layer. These magnetic channels extend further into the following Al propagation layer and continue to confine and guide subsequent electrons. By the time the laser interacts with its peak intensity, the majority of fast electrons flow through the center region, i.e., $Y \approx 60\text{-}100\mu\text{m}$. The confined flow of electrons in the center gives rise to a large transverse current gradient, that, combined with a high resistivity in Au, produces a global azimuthal field (30-50MG) that acts to further collimate fast electrons. It is also noted that at later time, strong B_z fields (50-60MG) due to the resistivity gradient $\partial B_z / \partial t = J_y (\partial \eta / \partial x)$ [26] are also observed at the Al/Au interface that are favorable for collimating the later arriving electrons. The cumulative effect of magnetic field induced collimation is clearly seen in Fig. 3(c) and Fig. 3(d) where the fast electron beam has a narrow spread with a reduced angular spread.

As discussed above and shown in Fig 3(c), fast electron flux (time integrated over the laser duration) in the central $20\mu\text{m}$ radius region after the Au transport layer is at a similar level to that in the Al target. Detailed examination of the time-resolved electron flux data in the simulations suggests a rather more dynamic evolution. Figures 5 (a) and (b) show comparison plots of the spatially resolved electron flux, time integrated up to 264fs and 396fs, respectively. At 264fs, before the peak of the laser pulse, the

transverse distribution profiles for the Al and Au targets are very similar with a slightly higher electron flux in the center region for the Al case, potentially due to stopping of relatively lower energy fast electrons produced at the rising edge of the laser pulse by collisions and drag in the high-Z Au layer. Just after the peak of the laser pulse at 396fs (Fig. 5(b)), guiding magnetic channels in the Au target are well established and electron flux in the central region of the target exceeds that in the Al case. The observed modulation in electron flux distribution also correlates well with the magnetic channel structure. During the falling edge of the laser pulse, fast electron flux through the center of the Au target drops below that in the Al target potentially due to both strong resistive electric field inhibition and the magnetic mirror effect, again particularly stopping low energy electrons. This is consistent with the observed strong localized energy deposition in the front Al layer of the Z=Au transport target in a small central region (Fig. 3(b)). As a result, over the whole duration of the laser pulse (726fs), electron flux remains similar to that in the Al case.

The PICLS simulated reduction (24%) in total number of electrons in the Au transport target is smaller than what observed in the experiment (56% reduction in total $K\alpha$ yield). There are several reasons that may contribute to this difference. The simulations were performed in a 2D Cartesian geometry using a simple Gaussian intensity distribution in a 10 μ m spot and a temporal pulse shape with a relatively sharp rise (330fs), which is quite different from a real 3D experiment. A more accurate laser intensity distribution $I(r, t)$ characterized on full energy shots shows a much larger low-intensity wing region in the focal spot and also a longer pulse rise time [27]. Including the wings (spatial and temporal) of the pulse while still injecting the same total energy in simulations would result in more low energy electrons that would be more effectively stopped in the Au transport target. In the experiment there is also an additional 100 μ m Al propagation layer between the Z-transport layer and the Cu tracer layer, which is beyond our computational capability. Nonetheless, the trend is well established and the simulated spread of the time integrated electron beam flux is in excellent agreement with the experiment.

In summary, we have directly shown that fast electron transport inside solid targets strongly depends on the transport material. A high- or mid-Z transport layer a few μ m beneath the front low-Z interaction layer collimates fast electrons, as compared to a low-Z aluminum transport layer, and

maintains the electron flux within a 20 μ m radius central spot. 2D collisional PIC modeling results are in excellent agreement with the experiment and show that resistive field effects, rather than scattering, dominate fast electron transport. Strong resistive B-field channels and global fields can confine and guide fast electrons with an initially large divergence. This work is very promising for cone-guided FI and provides a good foundation for future studies employing different transport and source layer materials. In addition, it has important implications for FI relevant pulse conditions where a higher flux of electrons could be transported to the fuel core via the guiding magnetic channels formed during the leading edge (with the sub-ps time scale) of the 10 ps high intensity pulse.

This work was performed under the auspices of the U.S. DOE under contracts DE-FG02-05ER54834 (ACE) and DE-FC02-04ER54789 (FSC). We acknowledge the assistance of D. Batani, J. Bonlie, H. Chen, R. Combs, R. Fedosejevs, H. Friesen, L. Gizzi, D.S. Hey, D. Higginson, J. Jaquez, L. C. Jarrott, P. Koester, A. Link, V. Ovchinnikov, J. Pasley, D. Price, B. Westover and L. Van Woerkem with performing the experiment.

*weims@fusion.gat.com

References:

1. M. Tabak *et al.*, Phys. Plasmas **1**, 1626 (1994).
2. A. A. Solodov *et al.*, Phys. Plasmas **15**, 112701 (2008)
3. S. Atzeni *et al.*, Plasma Phys. Control. Fusion **51**, 015016 (2009).
4. A. R. Bell and R. J. Kingham, Phys. Rev. Lett. **91**, 35003 (2003).
5. L. Gremillet *et al.*, Phys. Plasmas **9**, 941 (2002).
6. A. R. Bell *et al.*, Plasma Phys. Control. Fusion **39**, 653 (1997).
7. J. J. Honrubia, *et al.*, Laser Part. Beams **22**, 129 (2004).
8. J. A. Koch *et al.*, Phys. Rev. E **65**, 016410 (2001).
9. J. J. Santos *et al.*, Phys. Rev. Lett. **89**, 25001 (2002).
10. M. H. Key *et al.*, Phys. Plasmas **5**, 1966 (1998).
11. Y. Sentoku *et al.*, Phys. Rev. Lett. **107**, 135005 (2011).
12. F. Pisani *et al.*, Phys. Rev. E **62**, 5927 (2000).
13. T. Johzaki *et al.*, Plasma Phys. Controlled Fusion **51**, 014002 (2009).
14. B. Ramakrishna, Phys. Rev. Lett. **105**, 135001 (2010)
15. R.H.H. Scott *et al.*, Phys. Rev. Lett. **109**, 015001 (2012).
16. R. B. Stephens, Phys. Rev. E **69**, 066414 (2004).
17. P. M. Nilson *et al.*, Phys. Plasmas **15**, 056308 (2008).
18. C. Hombourger, Journal Phys. B **31**, 3693 (1998).

19. J. P. Santos *et al.*, J. Phys. B **36**, 4211 (2003).
20. C. Reich *et al.*, Phys. Rev. Lett. **84**, 4846 (2000).
21. J. A. Koch *et al.*, Rev. Sci. Inst. **74**, 2130 (2003).
22. K. U. Akli *et al.*, JINST **5**, P07008 (2010).
23. Y. Sentoku and A. Kemp, J. Comp. Phys. **227**, 6846 (2008).
24. M. M. Marinak *et al.*, Phys. Plasmas **5**, 1125 (1998).
25. A. Debayle *et al.*, Phys. Rev. E **82**, 036405 (2010).
26. A. R. Bell *et al.*, Phys. Rev. E **58**, 2471 (1998).
27. Y. Ping, *et al.*, Phys. Rev. Lett. **109**, 145006 (2012).

Figure captions:

FIG.1 (color online). Layout of the target, laser and diagnostics. Target layer thicknesses are in μm . The laser was incident at 17° from target normal. The $K\alpha$ imager was located 40° below the rear target normal and the HOPG x-ray spectrometer was 31° from the target normal in the equatorial plane.

FIG. 2 (color online). Cu $K\alpha$ images (a) and (b) from $Z=\text{Al}$ and $Z=\text{Au}$ transport targets respectively, the corresponding lineouts (c) and the total integrated $K\alpha$ yields (d) from the HOPG x-ray spectrometer for three types of transport targets. The images have the same spatial and color scales. $K\alpha$ intensity is normalized to the laser energy in (c) and to both the laser energy and solid angle in (d). Lineouts in (c) in bold are averaged over 2 data points per material. Shaded area between raw data lineouts (lighter lines) shows variation in data. Inset shows $Z=\text{Al}$ and $Z=\text{Au}$ lineouts only in a zoomed in region of interest.

FIG. 3 (color online). Electron energy density contour plot of (a) Al and (b) Au transport targets at the end of the laser pulse (726fs). The plot shows electrons in the pre-plasma region (starting with $X=10\mu\text{m}$) and solid density target (from $X=20\mu\text{m}$). For spatially resolved electron flux (c) and mean propagation angle (d) plots, electrons $>100\text{keV}$ are sampled in a $160\mu\text{m}$ wide, $2\mu\text{m}$ width box (marked between the dashed lines in (a) and (b)).

FIG. 4 (color online). Contour plots of the quasi-static magnetic fields (a), (b) at 198fs and (c), (d) at 726fs for $Z=\text{Al}$ and $Z=\text{Au}$ transport targets respectively.

FIG. 5 (color online). Time integrated electron flux distribution from the sampling box for Al and Au targets up to (a) 264fs (before the peak intensity) and (b) 396fs (at the laser pulse peak).

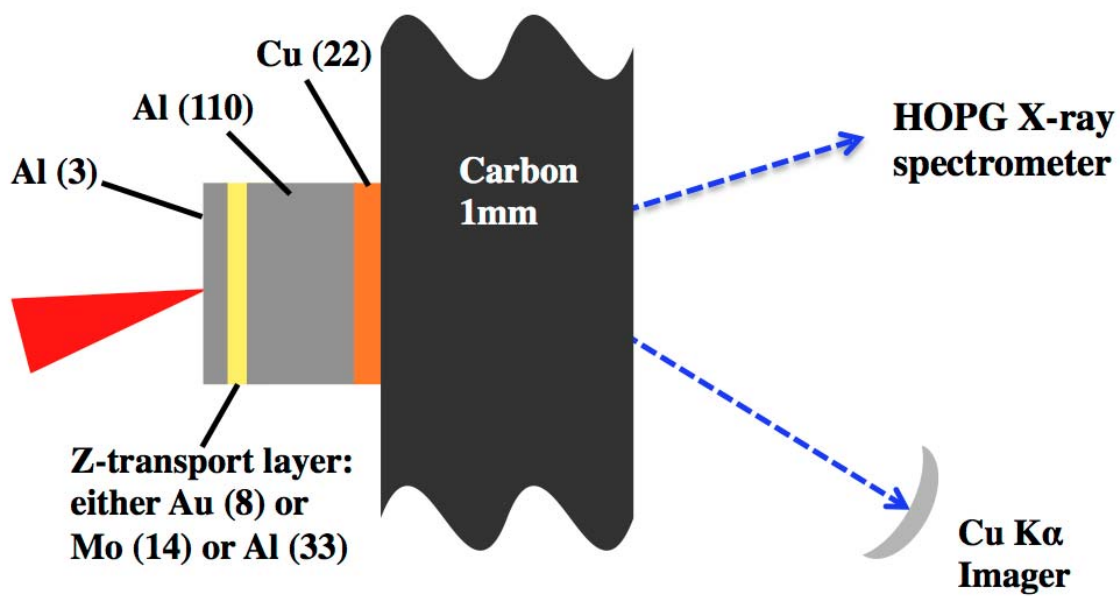


FIG. 1 Chawla *et al*

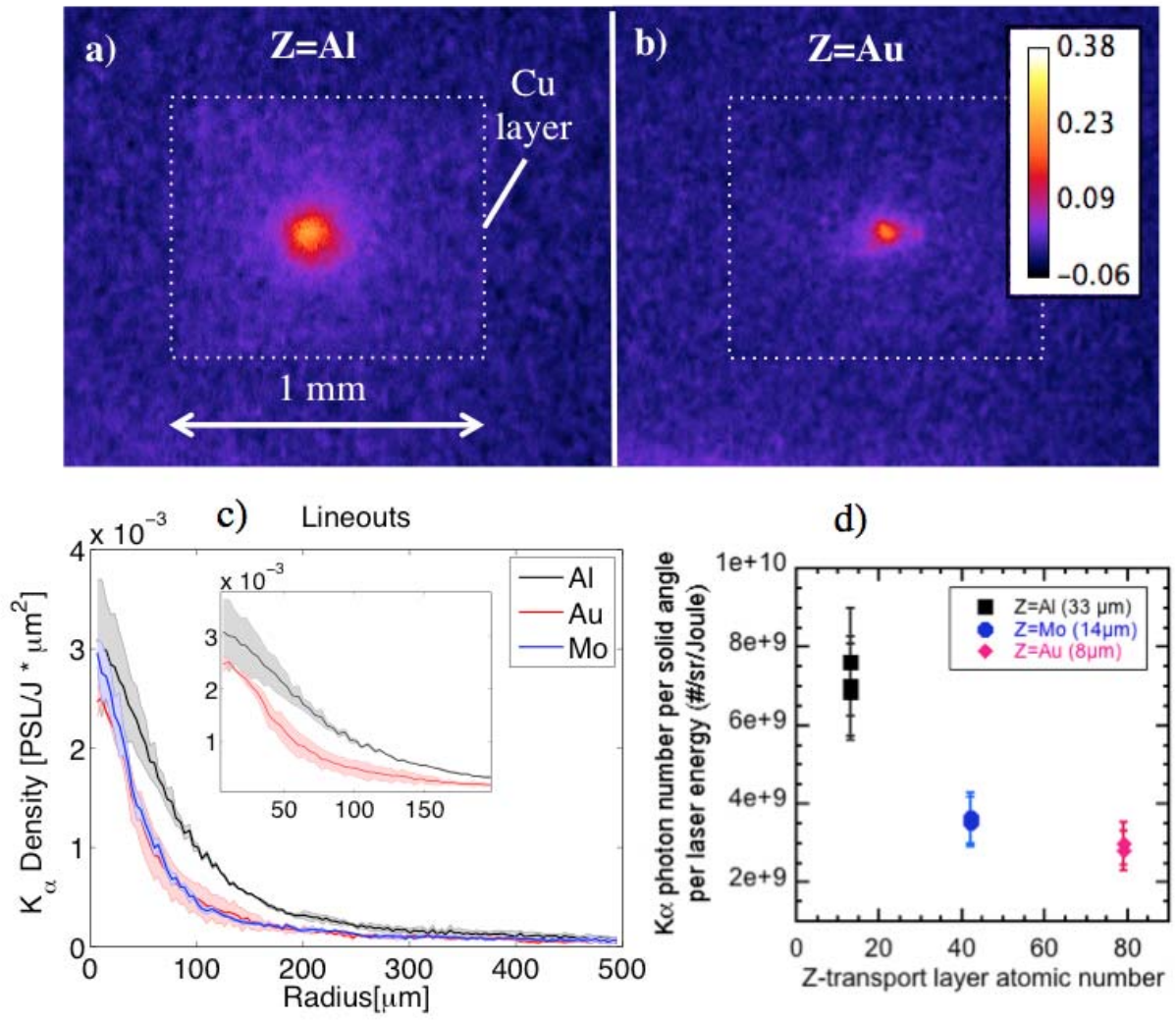


FIG. 2 Chawla *et al*

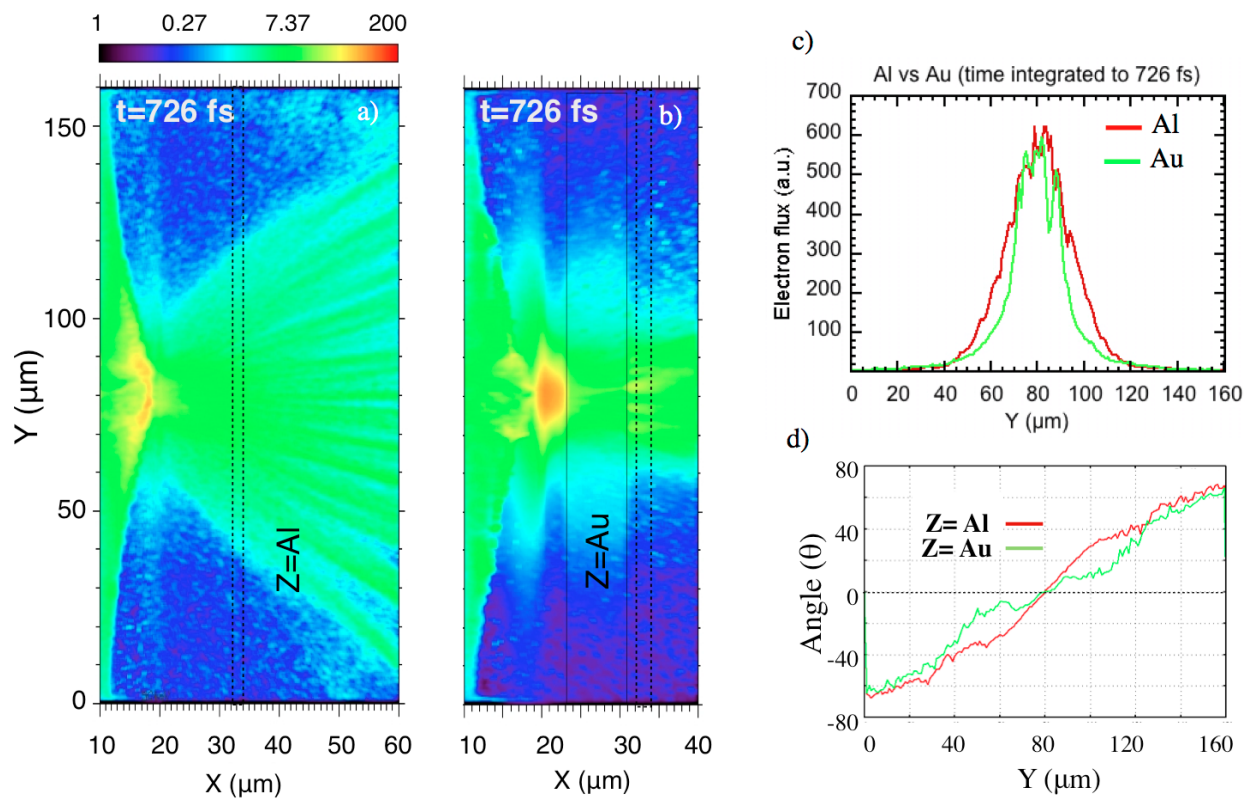


FIG. 3 Chawla *et al*

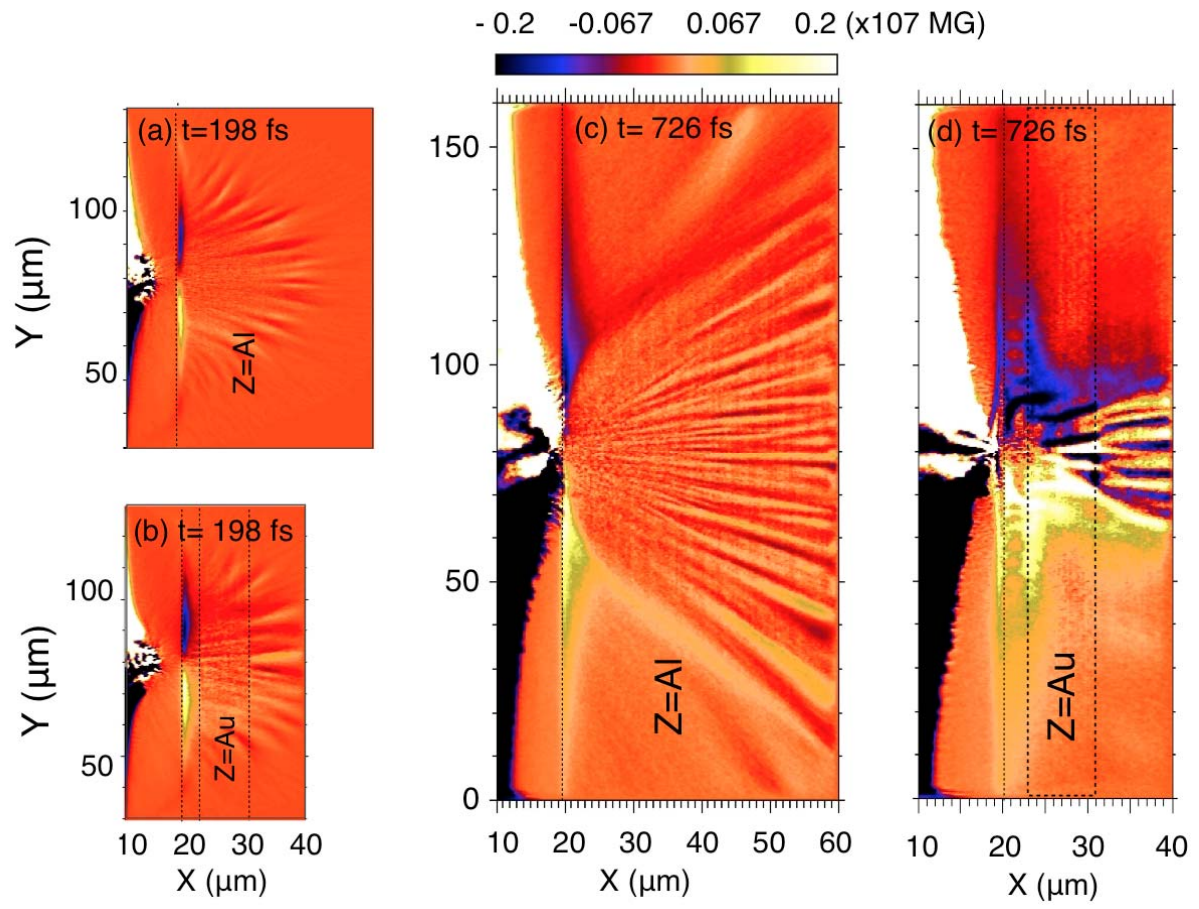


FIG. 4 Chawla *et al*

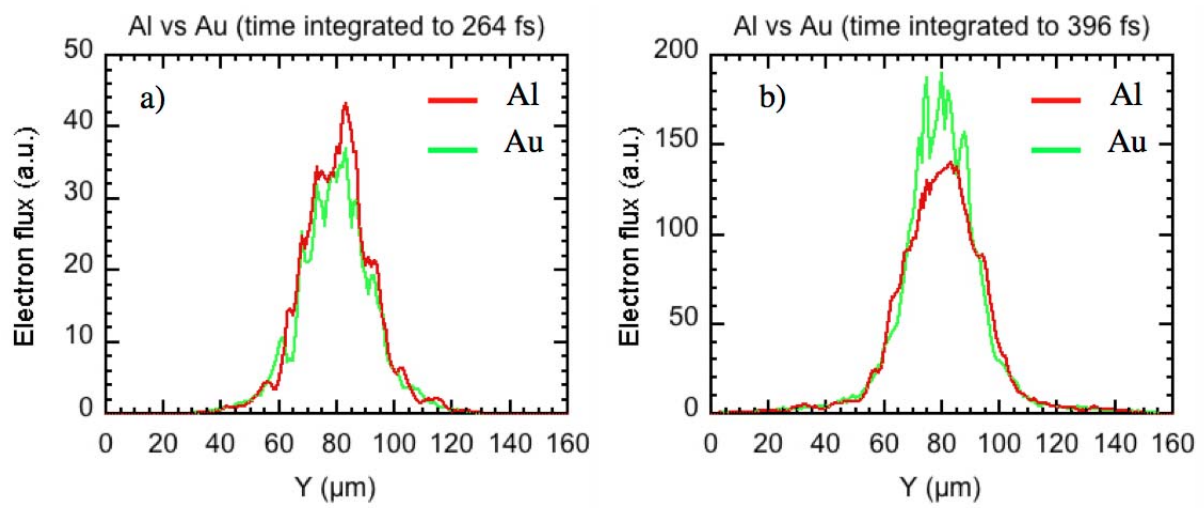


FIG. 5 Chawla *et al*